

SMALL-SIGNAL MODELING OF MAGAMP PWM SWITCH

Milan M. Jovanović and Laszlo Huber

DELTA Power Electronics Lab., Inc.
1872 Pratt Drive, Suite 1400
Blacksburg, VA 24060

Abstract- Circuit-based, small-signal models of the magamp which include the effects of the non-ideal squareness of the magamp's core B-H curve are derived for both the voltage-reset and current-reset control techniques. Since in this modeling approach the small-signal behavior of the magamp is described by equivalent circuits, circuit simulators can be easily used to facilitate the control-loop design optimization of the magamp.

1 Introduction

The magnetic amplifier (magamp) technique is one of the most reliable and cost-effective post-regulation methods for multiple-output power supplies. This is especially true for high-current post-regulated outputs since at higher output currents the efficiency of linear post-regulators is unacceptably low, while the complexity of more efficient switch-mode post-regulators is associated with a significant cost. Although in the past the magamps were used in numerous applications, their usage has dramatically increased with the introduction of 3.3-V integrated circuits (ICs). Namely, in today's data-processing equipment, which is based on both 3.3-V and 5-V ICs (mixed-power designs), it is necessary to provide at least two high-current, tightly regulated outputs. The most cost-effective approach to meeting the tight-regulation requirements at both outputs is to directly regulate the 5-V output and post-regulate the 3.3-V output using a magamp. Very often, in computer power supplies, the regulation requirements on the 12-V output, which is mainly used for driving the storage disk(s), warrant the use of a second magamp. As a result, today's multiple-output power supplies are complex control systems which contain multiple control loops that require suitable small-signal models for the control-loop performance optimization as well as for the analysis of possible loop interactions [1].

Various issues related to the operation, design, modeling, control, and simulations of magamps were discussed in [2] - [11]. However, while the operation of

magamps with non-ideal magamp-core materials was analyzed in [2] and [3], the small-signal analysis, modeling, and simulations of magamps have been, so far, exclusively carried out under the assumption of the ideal squareness of the B-H curve of magamp's core material [4]-[11].

The objective of this paper is to introduce accurate, circuit-based, small-signal models of magamps which include the effects of the non-ideal squareness of magnetic-core materials. Since, in this approach, the small-signal behavior of magamps is described by equivalent circuits, circuit simulators, such as Spice and Saber, can be easily used to facilitate the control-loop design optimization of magamps as well as to perform their loop-interaction analysis.

2 Key Waveforms of Non-ideal Magamp

A simplified circuit diagram of a typical, two-output forward converter with a magamp post regulator is shown in Fig. 1. In this converter, the regulation of output voltage V_{o1} is achieved by a pulse-width modulation (PWM) of the duty cycle of the primary switch S, whereas output voltage V_{o2} is regulated by a local magamp feedback loop, which modulates the duration of the blocking time of magamp inductor L_{MA} . It should be noted that the output of the magamp reset circuit $x_{Control}$ is control voltage v_C for the voltage-type reset, and reset current i_R for the current-type reset [3].

Figure 2 shows the key waveforms of a non-ideal magamp with the voltage reset, whereas Fig. 3 shows the assumed non-ideal core B-H characteristics. The waveforms in Fig. 2 assume that load current $I_{o2} = \langle i_{LF2} \rangle$ is large compared to the magnetizing current of L_{MA} so that $i_{sec2} = i_{MA}$ is zero during the time intervals in which L_{MA} is not saturated, and that L_{F2} is large so that the i_{LF2} ripple is negligible. It should be noted that the above assumptions greatly simplify the derivations of the models without compromising their accuracy.

As can be seen from Fig. 3, due to a non-ideal

3 Small-Signal Modeling

The small-signal models of the magamp were derived using the PWM-switch approach introduced and described in [12]. In this approach, the small-signal characteristics of a converter power stage are derived by perturbing the average currents and voltages of a three-terminal PWM switch. Therefore, to apply this approach, it is necessary to identify the three-terminal PWM-switch structure of the magamp post regulator.

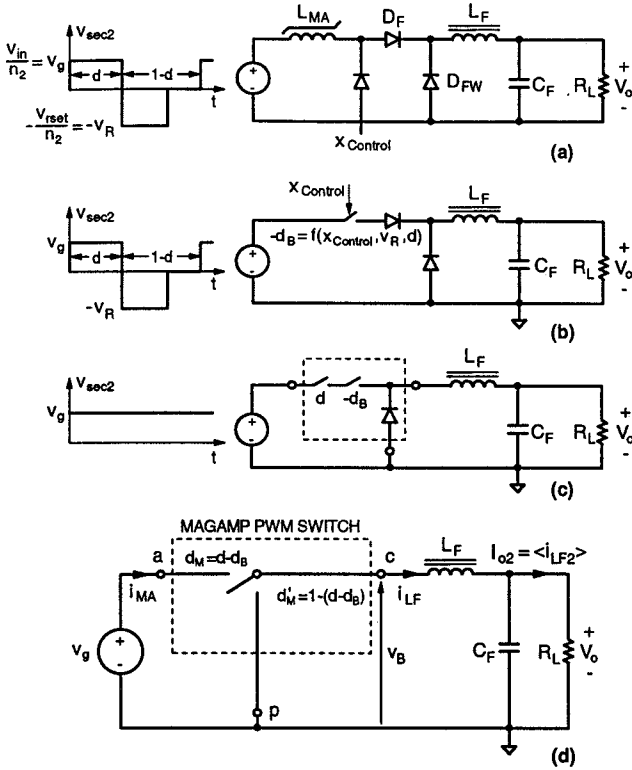


Fig. 4: Reduction of magamp to equivalent three-terminal PWM switch.

As can be seen from Fig. 2, the duty cycle of the voltage waveform at the input of the output filter, v_B , assuming $t_{rise}^{MA} = 0$ (i.e., ideal squareness), is a function of the primary-switch duty cycle $d = T_{ON}/T_S$ and the blocking duty cycle $d_B = T_B/T_S$. This dependence on d and d_B can be represented by an equivalent magamp PWM switch shown in Fig. 4(d), obtained by equivalent substitutions given in Figs. 4(a)-(c). As indicated in Fig. 4(b), generally, the blocking duty cycle d_B of the magamp is a function of control signal $x_{Control}$, reflected transformer reset voltage $v_R = v_{reset}/n_2$, and duty cycle d . The instantaneous (denoted with $\tilde{\cdot}$) and average (denoted with lower case letters) terminal voltages and currents of the three-terminal magamp PWM switch in Fig. 4(d) are shown in Fig. 5.

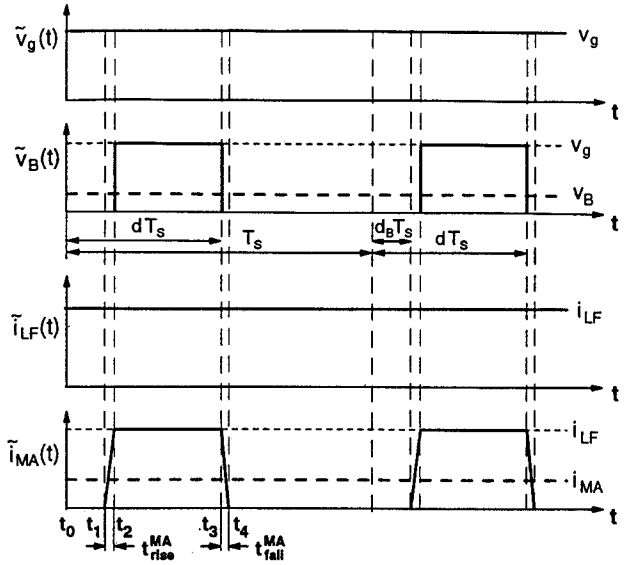


Fig. 5: Relationships between instantaneous and average terminal voltages and currents.

3.1 Power Stage Models

From Fig. 5, the relationships between the average terminal voltages and currents are:

$$v_B = v_g(d - d_B) - v_g \frac{t_{rise}^{MA}}{T_S}, \quad (1)$$

$$i_{MA} = i_{LF}(d - d_B) - \frac{i_{LF}}{2} \left[\frac{t_{rise}^{MA}}{T_S} - \frac{t_{fall}^{MA}}{T_S} \right], \quad (2)$$

where t_{rise}^{MA} and t_{fall}^{MA} are the rise and fall times of i_{MA} , respectively. From the i_{MA} waveform in Fig. 2, t_{rise}^{MA} and t_{fall}^{MA} can be written (using the notation in Fig. 2), as

$$\frac{t_{rise}^{MA}}{T_S} = \frac{n_2 i_{LF}}{v_{in}} L_{MA}^{sat} f_S = \frac{I_o Z_S}{v_g}, \quad (3)$$

$$\frac{t_{fall}^{MA}}{T_S} = \frac{n_2 i_{LF}}{v_{reset}} L_{MA}^{sat} f_S = \frac{I_o Z_S}{v_R}, \quad (4)$$

where $Z_S = L_{MA}^{sat} f_S$ is the saturation impedance of the magamp, $f_S = 1/T_S$ is the switching frequency of the primary switch, $I_o = i_{LF}$ is the output current, $v_g = v_{in}/n_2$ is the positive secondary-winding voltage at the magamp input (Fig. 2), and $v_R = v_{reset}/n_2$ is the negative (reset) secondary-winding voltage at the mag amp input (Fig. 2). It should be noted that for the RCD-reset method of the forward-converter transformer core, reset voltage v_R is constant, i.e., it is independent of input voltage v_g . On the other hand, for the active-clamp reset technique, v_R is dependent on v_g . To simplify the analysis, in the following derivations, it is assumed that v_R is constant, i.e., $v_R = V_R$. As a result, the derived models represent approximate

models for magamps operating in the forward converters with active-clamp reset.

Substituting Eqs. (3) and (4) in Eqs. (1) and (2), the average v_B and i_{MA} can be written as

$$v_B = v_g(d - d_B) - i_{LF}Z_S, \quad (5)$$

$$i_{MA} = i_{LF}(d - d_B) - \frac{1}{2}i_{LF}^2Z_S \left[\frac{1}{V_g} - \frac{1}{V_R} \right]. \quad (6)$$

By perturbing the average quantities in Eqs. 5 and 6 around their dc values (denoted with uppercase letters), *i.e.*, by setting $v_g = V_g + \hat{v}_g$, $v_B = V_B + \hat{v}_B$, $d = D + \hat{d}$, $d_B = D_B + \hat{d}_B$, $i_{MA} = I_{MA} + \hat{i}_{MA}$, and $i_{LF} = I_{LF} + \hat{i}_{LF}$, where $\hat{\cdot}$ denotes a small-signal perturbation, the dc and small-signal models can be obtained.

From the perturbed Eqs. 5 and 6, after a number of simple algebraic operations, the dc model of the magamp can be extracted as

$$I_{MA} = I_{LF}(D - D_B) - \frac{1}{2}I_{LF}^2Z_S \left[\frac{1}{V_g} - \frac{1}{V_R} \right] \quad (7)$$

$$V_B = V_g(D - D_B) - I_{LF}Z_S, \quad (8)$$

whereas, the small-signal model, after the second-order terms are neglected, is

$$\hat{i}_{MA} = I_{LF}(\hat{d} - \hat{d}_B) + \hat{i}_{LF}(D - D_B) \quad (9)$$

$$-I_{LF}Z_S \left[\frac{1}{V_g} - \frac{1}{V_R} \right] \hat{i}_{LF} + \frac{1}{2} \left(\frac{I_{LF}}{V_g} \right)^2 Z_S \hat{v}_g,$$

$$\hat{v}_B = V_g(\hat{d} - \hat{d}_B) + \hat{v}_g(D - D_B) - Z_S \hat{i}_{LF}. \quad (10)$$

The set of equations describing the dc model can be represented by the equivalent circuit shown in Fig. 6, whereas the set of equations describing the small-signal model can be represented by the equivalent circuit shown in Fig. 7.

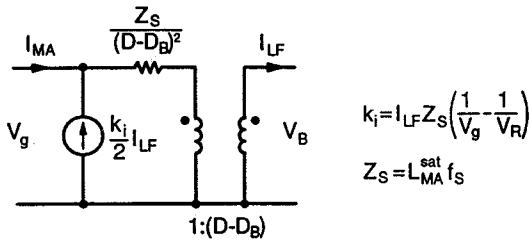


Fig. 6: Dc equivalent-circuit model magamp with non-ideal core.

As can be seen from Fig. 6, the effect of the non-ideal squareness of the core on the dc behavior of the magamp is modeled by the saturated inductance $Z_S/(D - D_B)^2$ and the current source $1/2Z_S(1/V_g - 1/V_R)I_{LF}^2$. Since impedance Z_S is connected in series

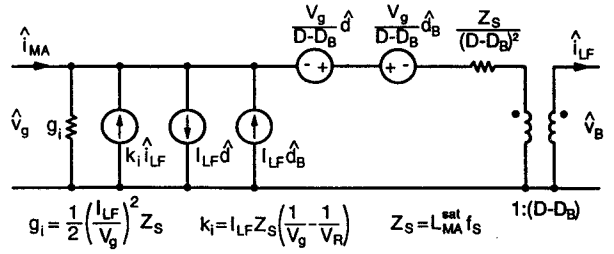


Fig. 7: Small-signal equivalent-circuit model of magamp with non-ideal core.

with the input and output terminals of the model, it makes the dc output voltage of the non-ideal magamp dependent on the output current. Similarly, as can be seen from Fig. 7, the effect of the non-ideal squareness of the core on the small-signal behavior of the magamp is modeled by impedance $Z_S/(D - D_B)^2$, current source $I_{LF}Z_S(1/V_g - 1/V_R)\hat{i}_{LF}$, and conductance $g_i = 1/2(I_{LF}/V_g)^2Z_S$. Due to Z_S and g_i , the small-signal transfer functions of the non-ideal magamp are damped. This damping is not accounted for when ideal magamp core characteristics are assumed. It should be noted that the ideal dc and small-signal magamp models can be obtained from the models in Figs. 6 and 7 by setting $Z_S=0$.

The small-signal equivalent circuit shown in Fig. 7 can be modified to include control variable $\hat{x}_{Control}$ instead of \hat{d}_B . To make this modification, it is necessary to find the functional relationship between control signal $x_{Control}$ and blocking duty cycle d_B . Generally, this functional relationship depends on the type of the magamp core reset circuit. The magamp reset circuit shown as a block in Fig. 1 can be implemented either by using the voltage reset of the magamp core, shown in Fig. 8(a), or the current reset, shown in Fig. 8(b). In the voltage-reset circuit, control voltage v_C , which is proportional to the error voltage v_{EA2} , is applied to the magamp core to obtain the desired core reset, *i.e.*, to obtain the desired blocking time t_B . In the current-reset circuit, reset current i_R , which is proportional to the error voltage, is used to control the magamp reset.

3.2 Voltage Reset

From the v_{MA} waveform in Fig. 2, which represents the voltage across the magamp inductor with the voltage reset, the volt-second (flux) balance during the blocking and resetting time intervals yields

$$\frac{v_{in}}{n_2}T_B + \frac{v_{in}}{n_2}t_{rise}^{MA} = \left(\frac{v_{rset}}{n_2} + v_C \right) T_{rset} - v_C t_{fall}^{MA}, \quad (11)$$

where T_{rset} is the reset time of the transformer core. This reset time can be calculated from the volt-second

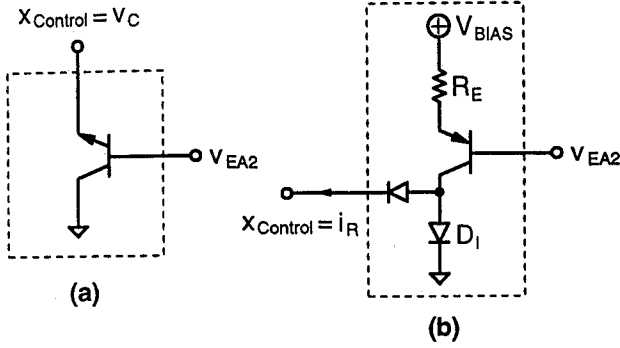


Fig. 8: Magamp reset circuit implementations: (a) voltage reset; (b) current reset.

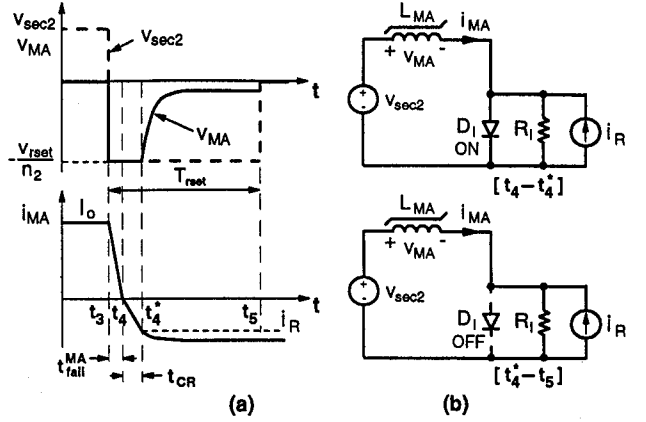


Fig. 10: Magamp with current reset: (a) v_{sec2} , v_{MA} , and i_{MA} waveforms; (b) topological stages during reset time. Note that reset current (negative i_{MA}) is much smaller than the load current so that it can be neglected. In this figure, it is shown much larger for clarity.

3.3 Current Reset

The major difference between the current reset and voltage reset of the magamp is seen in the magamp voltage waveform v_{MA} during the magamp reset interval. Figure 10 shows the v_{sec2} , v_{MA} , and i_{MA} waveforms of a magamp with the current reset, along with the equivalent circuits of the magamp during different phases of the reset. The other waveforms of the magamp with the current reset are identical with those for the voltage reset shown in Fig. 2. It should be noted that in Fig. 10(b) the current reset circuit shown in Fig. 8(b) is modeled by an ideal current source i_R with output resistance R_I in parallel.

As can be seen from Fig. 10(a), the reset period can be divided into three intervals. During the $[t_3 - t_4]$ interval, i_{MA} linearly decreases from I_o towards zero and $v_{MA} = -v_{rset}/n_2$. In this interval, the behavior of the magamp with current reset is identical to that of the voltage reset. After i_{MA} reaches zero at $t = t_4$, diode D_I in the reset circuit in Fig. 8(b), continues to conduct i_R because the current through unsaturated L_{MA} can not increase (in the negative direction) instantaneously. Because of the diode conduction, $v_{MA} = -v_{rset}/n_2$, as shown in Fig. 10. When i_{MA} reaches i_R at $t = t_4^*$, diode D_I ceases conducting, and voltage v_{MA} starts exponentially decreasing with time constant $\tau = L_{MA}^{unsat}/R_I$, as shown in Fig. 10(a). At $t = t_5$, the transformer reset is finished so that

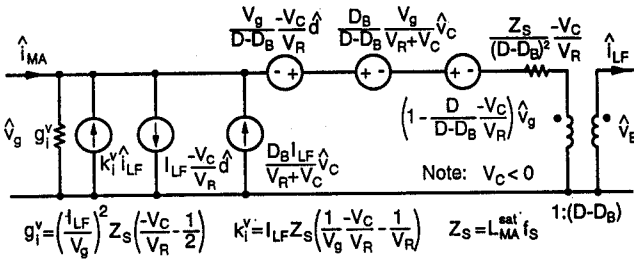


Fig. 9: Equivalent small-signal circuit of non-ideal magamp with voltage reset.

balance requirement of the transformer core, *i.e.*, from

$$v_{in} T_{on} = v_{rset} T_{rset}. \quad (12)$$

After substituting t_{rise}^{MA} and t_{fall}^{MA} from Eqs. 3 and 4 and T_{rset} from Eq. 12 in Eq. 11, the relationship between \hat{d}_B and \hat{v}_C can be derived as

$$\hat{d}_B = \left(1 + \frac{V_C}{V_R}\right) \hat{d} + \left(1 + \frac{V_C}{V_R}\right) \frac{Z_S I_o}{V_g^2} \hat{v}_g - \left(1 + \frac{V_C}{V_R}\right) \frac{Z_S}{V_g} \hat{i}_{LF} + \frac{D_B}{V_C + V_R} \hat{v}_C. \quad (13)$$

Using the relationship given in Eq. 13 to eliminate \hat{d}_B in the equivalent circuit in Fig. 7, the equivalent circuit, small-signal model of the magamp with voltage reset shown in Fig. 9 is obtained. Since all the dependent current and voltage sources in this model are controlled by currents or voltages, the implementation of this model in circuit simulators is easier compared to the model in Fig. 7, whose implementation requires additional modeling steps.

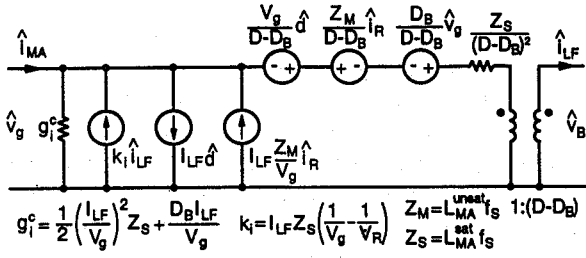


Fig. 11: Equivalent small-signal circuit of non-ideal magamp with current reset.

$v_{MA}=0$. It should be noted that the current reset requires that unsaturated inductance L_{MA}^{unsat} of magamp be finite, *i.e.*, that the slope of B-H curve in the unsaturated region be less than ∞ (non-ideal core).

Assuming that $\tau \ll T_{rset}$, *i.e.*, assuming that the reset circuit in Fig. 8(b) approaches an ideal current source, the approximation of the volt-second balance on L_{MA} can be obtained from the v_{MA} waveform in Figs. 2 and 10(a) as

$$\frac{v_{in} T_B}{n_2} + \frac{v_{in} t_{rise}^{MA}}{n_2} = \frac{V_{rset} t_{fall}^{MA}}{n_2} + \frac{V_{rset} t_{CR}}{n_2}, \quad (14)$$

where t_{CR} is calculated from Fig. 10(b) when diode D_I is conducting as

$$t_{CR} = \frac{L_{MA}^{unsat} i_R}{V_{rset}/n_2} = \frac{L_{MA}^{unsat} i_R}{V_R}. \quad (15)$$

Substituting t_{rise}^{MA} and t_{fall}^{MA} from Eqs. 3 and 4, and t_{CR} from Eq. 15 into Eq. 14, the small-signal relationship between \hat{d}_B and \hat{i}_R can be derived as

$$\hat{d}_B = \frac{Z_M}{V_g} \hat{i}_R - \frac{D_B}{V_g} \hat{v}_g. \quad (16)$$

Using the relationship in Eq. 16 to eliminate \hat{d}_B in equivalent circuit in Fig. 7, the equivalent circuit, small-signal model of the magamp with current reset shown in Fig. 11 is obtained.

It should be noted that the presented models do not take into account the phase-shift of the magamp modulator [4]. As a result, they are only accurate at frequencies at which the modulator phase shift can be neglected. Since for practical magamp implementations the modulator phase shift becomes important at frequencies above the crossover frequencies of the magamp loop, the derived models are quite accurate in predicting the close loop behavior of practical magamps. If necessary, the modulator phase shift as well as the B-H curve dynamic resistance [4], [5] can be incorporated into the models.

Finally, it should be noted that the modulator gain of the primary switch and its circuit implementations are discussed in [13] and [14].

4 Model Verification

The experimental verifications of the derived models were performed on an off-line, 100-W, two-output power supply implemented with a 100 kHz, forward-converter power stage. The main output, implemented with the current-mode control, is rated at $V_{o1}=5$ V and $I_{o1}=16$ A, whereas the rating of the magamp output is $V_{o2}=3.3$ V and $I_{o2}=6$ A.

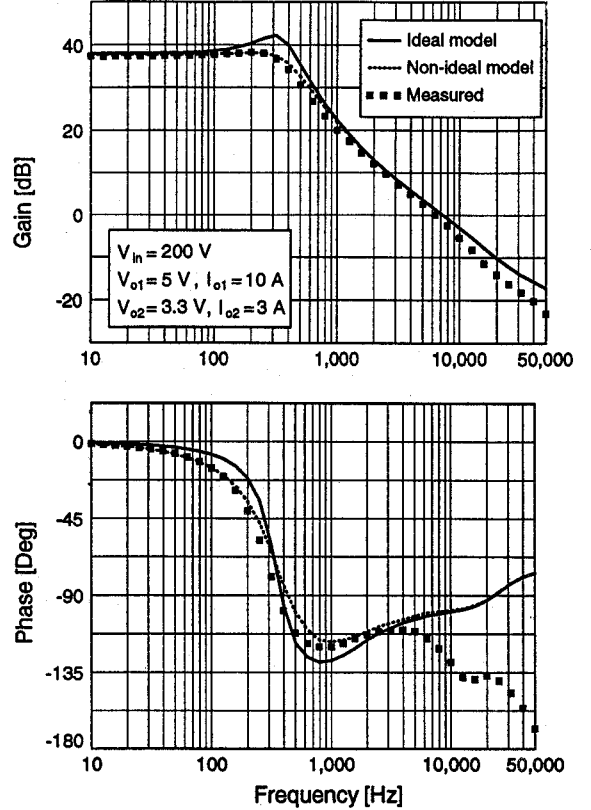


Fig. 12: Measured and calculated small-signal control-to-output transfer functions for experimental magamp with current reset. Main-loop crossover frequency $f_C=8.5$ kHz, magamp-loop crossover frequency $f_C^{MA}=2.5$ kHz.

Figure 12 shows the measured and calculated (ideal and non-ideal) control-to-output \hat{v}_{o2}/\hat{i}_R characteristics of the magamp with current reset. As it can be seen, the measured amplitude and phase characteristics are in very good agreement with the corresponding theoretically calculated characteristics obtained using the proposed non-ideal magamp small-signal model. The proposed non-ideal model accurately models the damping of the control-to-output transfer function. The discrepancy between the measured phase and the predicted phase which is observed at frequencies above 5 kHz is caused by the phase shift of the modulator, which is not included in the model given in Fig. 11.

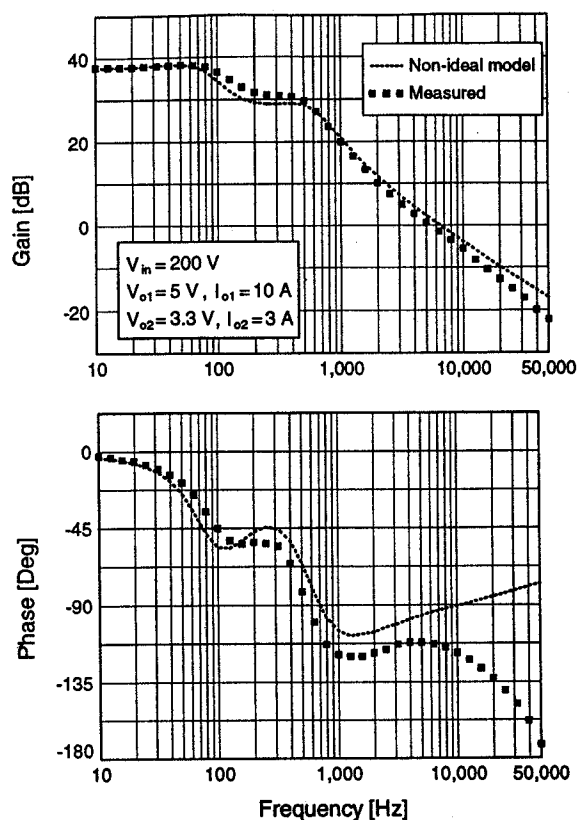


Fig. 13: Measured and calculated small-signal control-to-output transfer functions for experimental magamp with current reset. Main-loop crossover frequency $f_C = 0.1$ kHz, magamp-loop crossover frequency $f_C^{MA} = 2.5$ kHz.

Because the crossover frequency of the main loop of 8.5 kHz is higher than that of the magamp loop which is approximately 2.5 kHz, no measurable interaction between the loops is noticeable in Fig. 12.

If the crossover frequency of the main loop is reduced below the crossover frequency of the magamp loop, the two loops exhibit strong interactions. Figure 13 shows the calculated and measured control-to-output \hat{v}_{o2}/\hat{i}_R transfer functions of the experimental converter when the crossover frequency of the main loop is reduced to 0.1 kHz, i.e., below the crossover frequency of the magamp loop. As can be seen from Fig. 13, the main loop affects the magamp control-to-output of the magamp by reducing its gain in the 80-500 Hz range. The agreement between the calculated and measured gain is very good up to 10 kHz, whereas the calculated and measured phase show good agreement up to approximately 6 kHz. Above 6 kHz, the modulator phase lag becomes significant.

5 Summary

Circuit-based, small-signal models of magamps which are suitable for the analysis of control-loop interactions in multiple-output power supplies are derived. The models include the effects of the non-ideal squareness of the magnetic-switch-core B-H curve and also account for the differences in small-signal characteristics of the voltage-reset and current-reset techniques. Since the small-signal behavior of magamps is described by equivalent circuits, circuit simulators can be easily used to facilitate the control-loop design optimization of the magamp.

References

- [1] C. Jamerson, A. Hosseini, "Techniques for Reduction of Control-Loop Interactions in Magamp Supplies," *Magnetics Inc.*, Application Note, 1995.
- [2] C. Mullett, R. Hiramatsu, "An Improved Parallel Control Circuit for Saturable Reactor Output Regulators in High-Frequency Switch-Mode Converters," *IEEE Applied Power Electronics Conf. (APEC) Proc.*, pp. 99 - 106, 1986.
- [3] R.M. Tedder, "Effects of Converter Type, Reset Method, and Core Material on Magamp Regulator Performance," *IEEE Applied Power Electronics Conf. (APEC) Proc.*, pp. 391 - 400, 1989.
- [4] R.D. Middlebrook, "Describing Function Properties of a Magnetic Pulse-Width Modulator," *IEEE Power Electronics Specialists' Conf. (PESC) Rec.*, 1972.
- [5] T. Nabeshima, K. Harada, R. Hiramatsu, T. Kohchi, S. Komatsu, "On the Control of Magnetic Amplifier for High-Frequency Dc-to-Dc Converter," *IEEE Int'l Telecommunications Energy Conf. (INTELEC) Proc.*, pp. 449 - 454, 1985.
- [6] A.M. Urling, T.G. Wilson, H.A. Owen, G.W. Cromwell, J. Paulakonis, "Modeling the Frequency-Domain Behavior of Magnetic-Amplifier-Controlled High-Frequency Switched-Mode Power Supplies," *IEEE Applied Power Electronics Conf. (APEC) Proc.*, pp. 19 - 31, 1987.
- [7] C. Jamerson, "Calculation of Magnetic Amplifier Post Regulator Voltage Control Loop Parameters," *High-Frequency Power Conversion (HFPC) Conf. Proc.*, pp. 222 - 234, 1987.
- [8] D.Y. Chen, J. Lee, C. Jamerson, "A Simple Model Predicts Small-Signal Control Loop Behavior of Magamp Post Regulator," *High-Frequency Power Conversion (HFPC) Conf. Proc.*, pp. 69 - 84, 1988.
- [9] I.J. Lee, D.Y. Chen, Y.P. Wu, C. Jamerson, "Modeling of Control Loop Behavior of Magamp Post Regulators," *IEEE Int'l Telecommunications Energy Conf. (INTELEC) Proc.*, Paper 20.1, 1989.
- [10] V.J. Thottuvelli, "Using SPICE to Model the Dynamic Behavior of Dc-to-Dc Converters Employing Magnetic Amplifiers," *IEEE Applied Power Electronics Conf. (APEC) Proc.*, pp. 750 - 759, 1990.
- [11] D. Edry, S. Ben-Yaakov, "A SPICE Model of Magamp Post Regulators," *IEEE Applied Power Electronics Conf. (APEC) Proc.*, pp. 793 - 800, 1992.
- [12] V. Vorpérian, "Simplified Analysis of PWM Converters Using the Model of the PWM Switch: Part I and II," *IEEE Trans. Aerospace & Electronic Systems*, Vol. 26, No. 3, pp. 490 - 505, 1990.
- [13] R.B. Ridley, "A New, Continuous-Time Model for Current-Mode Control," *IEEE Trans. Power Electronics*, Vol. 6, pp. 271-280, Apr. 1991.
- [14] V. Vorpérian, "Analysis of Current-Mode Controlled PWM Converters Using the Model of the Current-Controlled PWM Switch," *Power Conversion & Intelligent Motion Conference (PCIM)*, pp. 183-195, 1990.